Pre-print submitted version

Enamine-based hole transporting materials for vacuum-deposited perovskite solar cells

Matas Steponaitis[a], Maria-Grazia La-Placa[b], İsmail Cihan Kaya[b], Giedre Bubniene[a], Vygintas Jankauskas[c], Maryte Daskeviciene[a], Michele Sessolo[b†], Tadas Malinauskas[a†], Henk J. Bolink[b] and Vytautas Getautis[a]

a. Department of Organic Chemistry, Kaunas University of Technology, Radvilenu pl. 19, LT-50254, Kaunas, Lithuania.

b. Instituto de Ciencia Molecular, Universidad de Valencia, C/Catedrático J. Beltrán 2, 46980 Paterna, Spain.

c. Institute of Chemical Physics, Vilnius University Sauletekio al.3, Vilnius LT-10257, Lithuania

† Corresponding authors: michele.sessolo@uv.es, tadas.malinauskas@ktu.lt

Abstract

In a short period of time rapid development of perovskite solar cells attracted a lot of attention in the science community with record for power conversion efficiency being broken every year. Despite the fast progress in power conversion efficiency there are still many issues that need to be solved before starting large scale commercial application, among others, the difficult and costly synthesis and usage of toxic solvents for the deposition of hole transport materials (HTMs). We report new enamine-based charge transport materials obtained via simple one step synthesis procedure, from commercially available precursors and without the use of expensive organometallic catalysts. The developed materials demonstrated rapid loss of mass during thermogravimetry analysis suggesting that they could be processed not only using solution processing, but also via vacuum deposition technique. Furthermore, all HTMs demonstrated high charge carrier mobility with H2 possessing the highest mobility of 2.5·10-2 cm2V-1s-1 at strong electric fields. The investigated materials were employed in vacuum-deposited p-i-n perovskite solar cells and champion devices with enamine H2 demonstrated PCE of 18.4%.

Introduction

The growth of human population and the technological progress in the last hundred years has dramatically increased the global energy consumption [1]. With limited fossil fuel resources and the overall rise in pollution, renewable energy sources have become an attractive alternative. One of the most promising alternatives are photovoltaic devices. In recent years the field of perovskite solar cells (PSCs) attracted large attention mostly due to the easily tuneable band gap of the perovskite [2], relatively simple device fabrication [3;4] and the continuously increasing power conversion efficiency (PCE) with current record being 25.2 % [5]. PSCs can be fabricated in two configurations, n-i-p or p-i-n, identified depending on the type of charge selective layer which is deposited onto the front transparent contact (in n-i-p and p-i-n, n- and p-type layers are used as the front contact, respectively). n-i-p devices usually use compact or mesoporous TiO2 or SnO2 [6;7;8;9] as the electron transport layer (ETL), deposited on transparent conductive oxide (TCO) substrates. On top of the ETL, the perovskite, a hole transport layer (HTL) and a metal cathode are subsequently deposited [10]. The main architectural differences between p-i-n and n-i-p PSCs are the materials used as ETL and HTL as well as the order in which they are deposited [11].

p-i-n PSCs have several advantages compared to n-i-p devices: i) the high temperature needed for TiO2 annealing is avoided; ii) low-cost copper can be used as a cathode instead of silver or gold [12]; iii) p-i-n architecture enables higher PCE potential in tandem cells due to lower parasitic absorption in the front contact [13, 14].

Currently some of the most widely used hole transport materials (HTMs) for p-i-n PSCs are (semi)conducting polymers such as poly-TPDs [15;16], PTAA [17;18], PEDOT:PSS [15;19] and metal oxides as CuOx [20;21], NiOx [20;22]. The aforementioned organic compounds are often deposited using spin-coating technique, which is cost wise very inefficient and not suitable for large-scale fabrication. As an alternative, perovskite solar cells can be fabricated by vacuum deposition, which is widely used in the industry and hence suitable to scale up the device preparation. Moreover, it avoids use of toxic solvents which are usually employed in the fabrication of PSCs [23] and allows to more accurately control the processing of multilayer stacks [24]. However, its application is limited to relatively small molecules as they need to be sublimed [25]. Herein new enamine-based HTMs were synthesized in a simple single step reaction from commercially available materials without the use of expensive transition metal catalysts. The compounds were synthesized in order to have a relatively large ionization energy, which should match the perovskite absorber to ensure efficient hole extraction. The HTMs exhibited high thermal stability and large carrier drift mobility, reaching 2.5·10-2 cm2V-1s-1 (H2) at strong

electric fields. All materials were tested in fully vacuum-processed p-i-n PSCs, showing performance comparable to state-of-the-art evaporated devices

Results and Discussion

Synthesis

Synthesis of enamines H1, H2, H3 and H4 was conducted using single-step acid catalysed condensation reaction. Carbazole was condensed with diphenylacetaldehyde using camphor-10-sulfonic acid (β) (CSA) as a catalyst in toluene to give enamine H1 (Scheme 1). The same reaction conditions were applied in case of m-tolidine to obtain H3 as desired product.

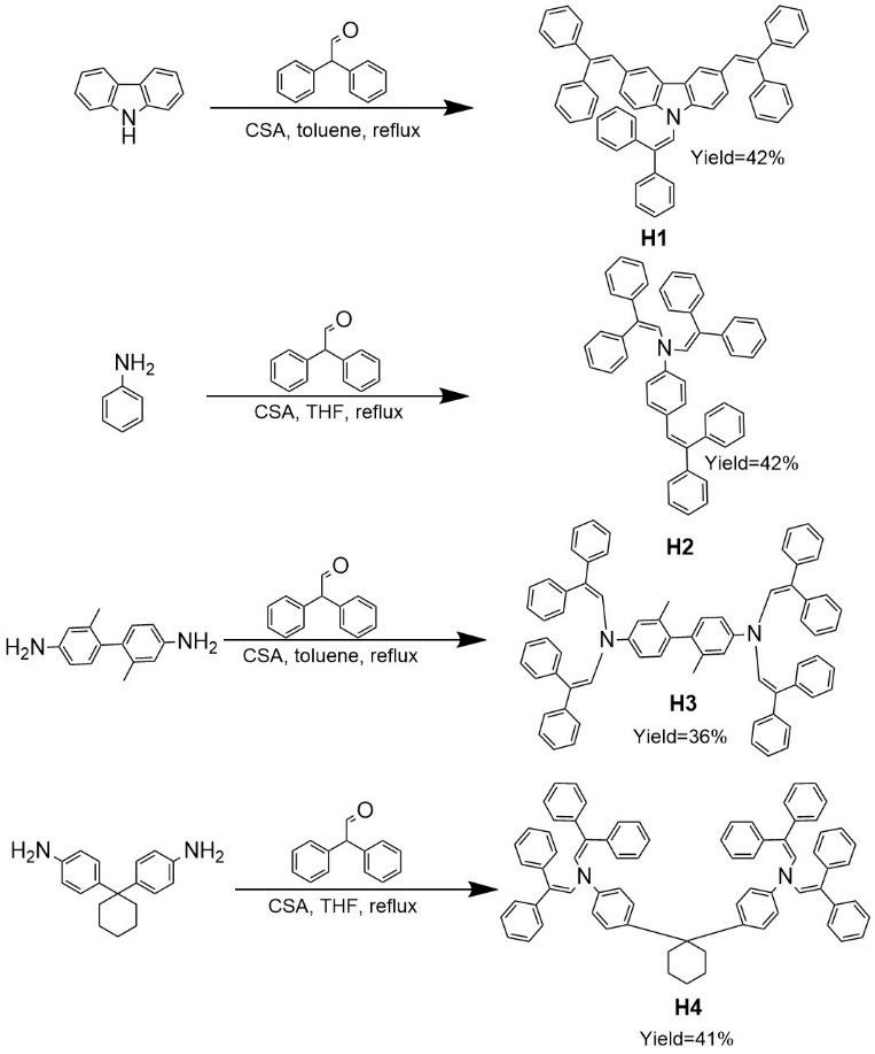

Scheme 1. Synthesis of enamine H1, H2, H3 and H4.

Enamines H2 and H4 were synthesized in the same type of one step condensation reaction of aniline or 1,1-bis(4-aminophenyl)cyclohexane with diphenylacetaldehyde utilizing CSA, although in this case THF was used as a solvent instead of toluene (Scheme 1). The mechanisms for the above mentioned reactions were reported in earlier publications [26;27].

After performing extraction H1 and H2 are purified by column chromatography, while H4 follows the same pattern except extraction is replaced with precipitation by pouring the cooled reaction mixture into methanol. HTM H3 requires the simplest purification: the cooled reaction mixture is poured into ethyl acetate and formed crystals are filtered and washed with methanol and ethyl acetate.

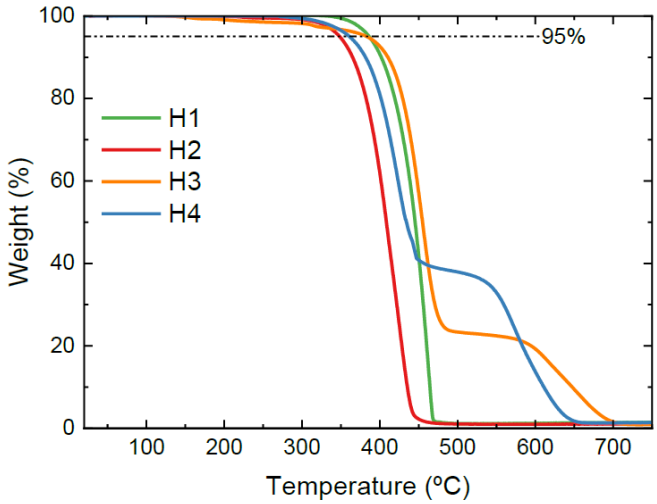

Figure 1. TGA heating curves of H1, H2, H3 and H4.

Thermal properties

Thermal stability of the materials was measured using thermogravimetric analysis (TGA) and the results can be seen in Figure 1 and Table 1. All tested HTMs showed 5% weight loss at temperatures higher than 300 °C, proving that they are sufficiently thermally stable for application in PSCs. Furthermore, the rapid weight loss seen in Figure 1 indicates that investigated materials can sublime and could be vacuum deposited.

Analysis of differential scanning calorimetry (DSC) data showed that materials H1, H2 and H4 have relatively high glass transition temperatures (Tg), above 100°C (Table 1). This might be

beneficial for the stability of PSCs under working conditions, when the temperature can exceed 65 □C [28]. The aforementioned compounds can be both amorphous and crystalline with melting temperatures (Tm) higher than 200°C for H1, H2. H4 demonstrates crystallization at 202□C and subsequent melting of the crystals at 315°C during first heating.

Table 1. Thermal characteristics of the HTMs.

Compound	T_g [a], °C	T_m [b], °C	T_{dec} [c], °C
H1	111	215	386
H2	110	235	348
H3	-	339	361
H4	156	315	383

a) Determined by DSC: scan rate = 10 °C min−1, N2 atmosphere; second run; b) Determined by DSC: scan rate = 10 °C min−1, N2 atmosphere; first run; c) Onset of decomposition determined by TGA: heating rate = 10 °C min−1, N2 atmosphere.

Interestingly m-tolidine derivative H3, is a crystalline material with Tm observed at 339°C. The lack of Tg could be explained by the spatial configuration of diphenylacetaldehyde substituents and the two methyl groups in the meta- position of m-tolidine fragment. Introduction of the structural symmetry in H3, compared with H2, leads to higher melting temperature and increased tendency to crystallize. It is verified by absence of glass transition during first and second heating runs, presence of exothermic crystallization peak at 239°C during rapid cooling and endothermic melting peak at 330°C during second heating run in DSC curves for H3 (Figure S1).

Optical and Photoelectrical properties

Light absorption and emission characteristics of HTMs H1, H2, H3 and H4 were measured in toluene solutions and on a glass substrate. Compounds H1 and H2 contain three phenylethenyl substituents and differ only by the central core (carbazole in H1 and aniline in H2), however that

is enough to influence optical properties. Differences in absorption spectra between these two materials are noticeable both in solution and on a glass substrate.

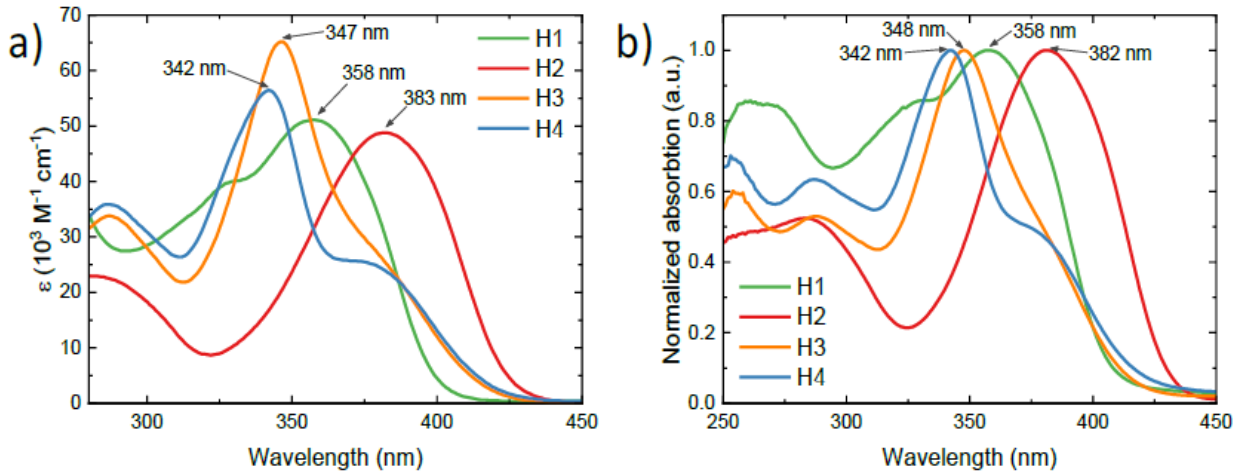

Figure 2. a) UV-vis absorption spectra of H1, H2, H3, H4 in toluene and b) thin-films on glass.

Observed redshift (□25 nm) in the UV-vis absorption spectra for the aniline derivative H2, compared with carbazole HTM H1 (Figure 2a; Figure 2b) could be explained by the structural difference of the central core of H1 and H2 [29;30]. The same tendencies can be seen for the emission spectra: after excitation, H1 emits shorter wavelength light than H2 (Figure S2; Figure S3).

Table 2. Absorption and photoluminescence (PL) data

Compound	λ_{max}^{abs}, nm [a]	λ_{max}^{abs}, nm [b]	PL, nm [c]	PL, nm [d]
H1	358	358	458	479
H2	383	382	470	495
H3	347	348	490	499
H4	342	342	496	494

a) Absorption maxima in toluene; b) Absorption maxima on glass substrate; c) Fluorescence maxima in toluene; d) Fluorescence maxima on glass substrate

H3 and H4 are structurally similar molecules both containing four phenylethenyl substituents connected via two aniline derivatives with the biggest difference being interruption of the conjugation in H4 by a cyclohexane fragment. The aforementioned separation has little effect on the absorption and emission properties when comparing H3 with H4 (Table 2). The most notable difference can be seen in the intensity of absorption in the solution, H3 demonstrates more intense absorption than H4 (Figure 2a) [29]. This could be explained by the slightly lower π-conjugation of H4 due to somewhat larger steric hindrances in the molecule compared to H3.

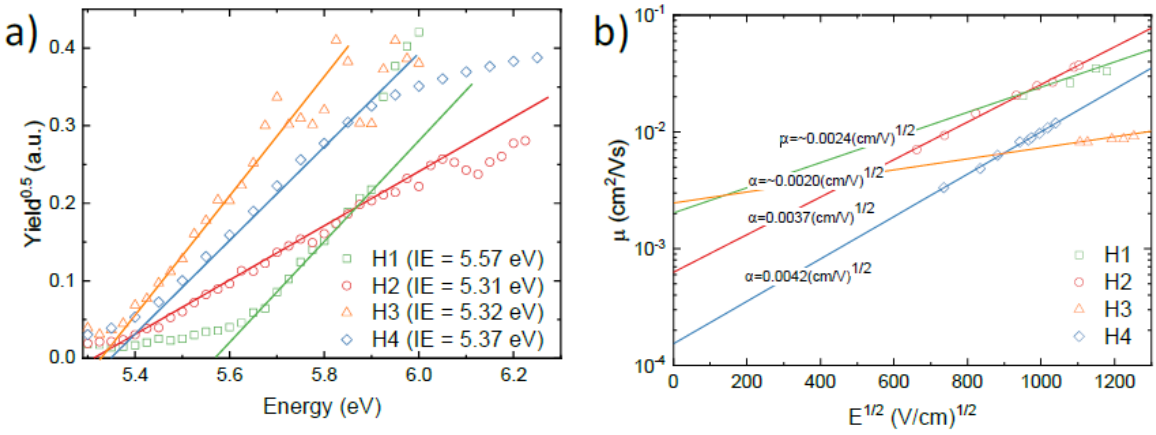

Figure 3. a) Ip measurements of compounds H1, H2, H3 and H4. b) Charge carrier mobility of the tested materials.

Ionization energy (Ip) of the investigated p-type semiconductors were measured by photoemission spectroscopy in air (Figure 3a). Materials H2, H3 and H4 have Ip values in the 5.30 – 5.40 eV range, while H1 has higher Ip of 5.57 eV (Table 3). The large difference of Ip between H2□H4 and H1 is most likely due to the fact that H1 contains carbazole fragment, while other tested HTMs can be viewed as aniline derivatives [29;30].

Compound	I_p, eV (a)	μ_0, cm^{2}V^{-1}s^{-1} (b)	μ, cm^{2}V^{-1}s^{-1} (c)	$\alpha^{(d)}$
H1	5.57	$2.1\cdot10^{-3}$	$2.3\cdot10^{-2}$	0.0024
H2	5.31	$6\cdot10^{-4}$	$2.5\cdot10^{-2}$	0.0037
H3	5.32	$2.4\cdot10^{-3}$	$7\cdot10^{-3}$	0.0020
H4	5.37	$1.5\cdot10^{-4}$	$1\cdot10^{-2}$	0.0042

a) Ionization energy was measured by photoemission spectroscopy in air from films; b) Hole mobility value at zero field strength; c) Hole mobility value at the electric field strength of 6.4·105 Vcm-1; d) Poole–Frenkel parameter.

Table 3. Photophysical properties of the synthesized materials.

The charge carrier mobility of HTMs was measured from films by xerographic time-of-flight (XTOF) method (Figure 3b). All materials displayed excellent charge transport properties, well above 1·10-3 cm2V-1s-1 (Table 3), rivalling some of the best organic HTMs used in PSCs [31]. The good drift carrier mobility of tested materials could be explained by more efficient charge hopping due to more favourable arrangement of molecules [32].

Device performance

Perovskite solar cells with the p-i-n configuration (Figure 4a) were prepared by vacuum deposition following previously published protocols (details in the Supplementary information) [33]. Briefly, glass slide with indium tin oxide (ITO) patterned electrodes were coated with MoO3 (5 nm), the hole transport layer (HTL, 10 nm), a 500 nm thick methylammonium lead iodide (MAPI) absorber, C60 (25 nm), bathocuproine (BCP, 8 nm) and silver (100 nm). MoO3 was used to increase the work function at the front electrode and enhance charge extraction from the HTL to the ITO [34]. All four HTLs were tested in devices, and at least 8 pixels were measured for each material.

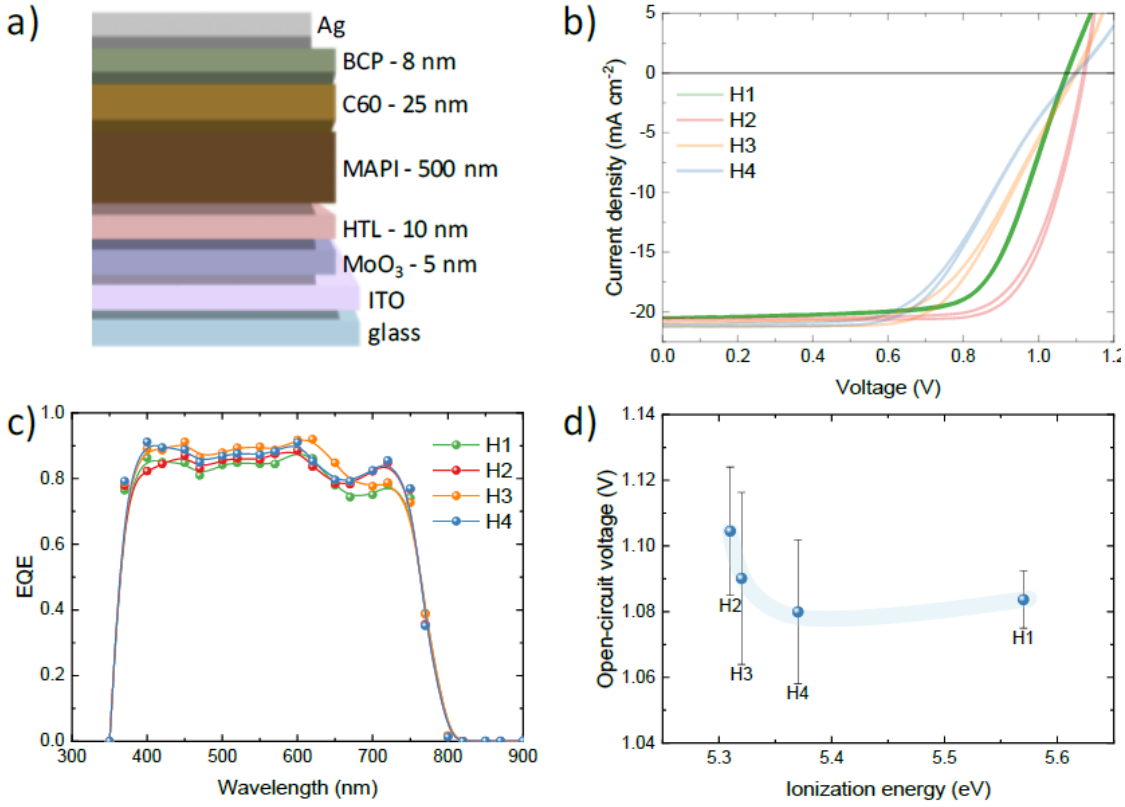

Figure 4. a) Solar cell layout with materials and corresponding film thickness. b) J-V curves under simulated solar illumination and c) EQE spectra for solar cells employing the different HTLs. d) Trend of the solar cells Voc as a function of the ionization energy of the HTL.

The solar cells were characterized by measuring the current density as a function of the applied voltage (J-V curves, Figure 4b), under simulated solar illumination, in forward (from short to open circuit) and reverse (from open to short circuit) bias. JV curves showed only small hysteresis between the forward and reverse bias, which might indicate the presence of interfacial recombination [35]. The characteristic photovoltaic parameters (extracted from the forward J-V scans) as a function of the HTL used are reported in Table 4. The short-circuit current Jsc was found to vary only in the 20.5-21 mA cm-2 range among the series of devices with different HTLs, due to their high transparency in the visible part of the electromagnetic spectrum. This is confirmed by the spectral response of the solar cells (external quantum efficiency, Figure 4c), which is similar for the entire series, fluctuating between EQE values of 0.8 and 0.9. More striking are the differences in fill factor (FF), which reflects the efficiency of the charge transport and extraction processes. Solar cells with H3 and H4 showed a pronounced kink in the J-V curve under illumination, which result in average FF limited to 56.8% and 53.8%, respectively.

Table 4. Photovoltaic parameter extracted from p-i-n solar cells employing different HTLs (10 nm thick).

HTL		J_{sc}, mA/cm²	V_{oc}, mV	*FF*, %	PCE, %
H1	*average*	20.5	1084	67.6	15.0
	best	20.5	1078	69.3	15.3
H2	*average*	20.5	1105	71.8	16.3
	best	20.8	1130	74.9	17.6
H3	*average*	20.8	1090	56.8	12.9
	best	21.2	1101	61.1	14.3
H4	*average*	20.8	1080	53.8	12.1
	best	21.1	1110	56.3	13.2

The FF was slightly higher for cells with H1, reaching 67.6% on average, and the maximum value was obtained when employing H2 as the HTL, with an average FF of 71.8% and as high as 74.9% for the best pixels. The origin of this trend is not clear, as we did not observe a correlation with the charge carrier drift mobility (Table 3) nor with the ionization energy of the materials. A more apparent trend was observed for the opencircuit voltage (Voc), which was found to scale inversely with the ionization energy of the HTLs (Figure 4d). This observation is likely related with the alignment of the highest occupied molecular orbital (HOMO) of the HTL (estimated by the

ionization energy) and the maximum of the valence band (VBM) of the perovskite. While the Voc of perovskite solar cells is rather insensitive to the HOMO of the HTLs [36;37], there is a consensus towards the need to minimize the energy barriers for charge extraction to maximize voltage and FF [38]. In this case, the higher photovoltage (1105 mV on average, with highest at 1130 mV) measured for H2 agrees with recent measurements of the VBM for MAPI, estimated at 5.2 eV from the vacuum level [39]. On the other extreme, solar cells employing H1 as the transport material (ionization energy > 5.5 eV) delivered Voc of approximately 1080 mV. The overall efficiency of the devices with H2 was found to be the highest in the series, with PCE of 16.3% on average and the best pixel at 17.6%. In view of the promising performance of H2 in our vacuum deposited perovskite solar cells, we have fabricated additional cells with thinner HTL (5 nm instead of 10 nm), as this might alleviate transport losses within the organic semiconductor and increase the built-in potential [36].

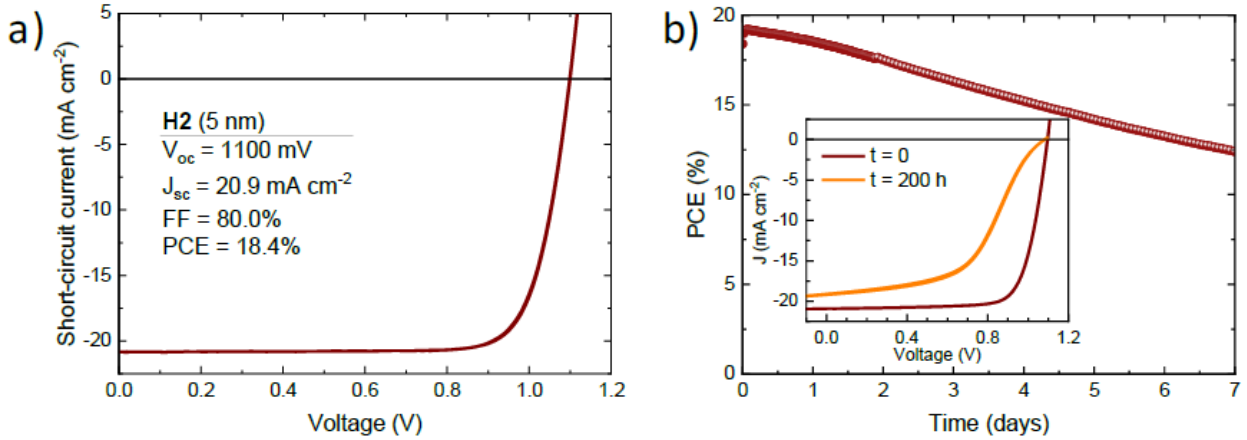

Figure 5. a) J-V curve of a representative solar cell using a 5 nm thick H2 film as the hole transport layer. b) Evolution of the efficiency measured under continuous illumination with maximum power point tracking over a week. The inset shows the J-V curves of the device before and after 200 hours of continuous illumination.

Solar cells with 5 nm thick H2 show a very good rectification, fully suppressed hysteresis and FF as high as 80%, maintaining essentially unvaried the other photovoltaic parameters (Figure 5a). The improvement in FF led to PCE as high as 18.4%, which is close to the highest reported for vacuum-processed p-i-n devices [33;40] (about 19%). We further tested the solar cells over time, under continuous simulated solar illumination. The devices were encapsulated with UV-curable resin and a glass slide and kept at 25 °C under a nitrogen flow (max relative humidity 10%), to minimize the effect of the environment. The maximum power point was continuously tracked and the evolution of the PCE over time is depicted in Figure 3b. The solar cell showed an initial rise

in efficiency (to about 19%) followed by a slow but continuous decay for the 7 days of characterization. After one week of continuous operation, the device with H2 contact delivered a PCE of 12.5%, which was found to be mainly determined by the decrease in FF (see inset in Figure 5b) and to a less extent by a lower current density. While the latter points towards a degradation of the MAPI perovskite film, we cannot exclude other degradation pathways related with interfacial effects at the front contact.

Cost estimation

To evaluate the cost-effectiveness of the best performing material H2, we calculated the estimated cost of its synthesis based on the procedure established by Osedach et al. (Table S1) [41]. Moreover, the cost of spiro-TTB, an often used p-type semiconductor in vacuum deposited PSCs [37], was calculated based on articles by M. L. Petrus et al. and Yin et al (Table S2) [42;43]. It was estimated that the cost of our HTM is about 19$ per gram which is less than 1/3 of spiro-TTB (about 67$ per gram). Furthermore, synthesis of H2 is done in a single step reaction and does not require expensive palladium catalysis, avoiding traces of organic impurities and catalyst residue that could act as photoquenchers or charge traps [44;45].

Conclusions

We have synthesized new enamine-based compounds using single step reaction without the use of expensive transition metal catalysts. Despite structural differences all HTMs displayed excellent charge transport properties with H2 reaching hole mobility 2.5·10-2 cm2V-1s-1 at strong electric fields. Furthermore, all materials exhibited relatively high Tg and Tm, great thermal stability and rapid weight loss during TGA, which allowed processing of these HTMs in p-i-n architecture PSCs via vacuum-deposition. H2 demonstrated the best PCE with the champion cell reaching 18.4% efficiency. Above-mentioned results and properties designate these compounds as attractive materials for large scale PSC applications.

Conflicts of interest

There are no conflicts to declare.

Acknowledgements

The research leading to these results had received funding from the European Union's Horizon 2020 research and innovation program under grant agreement No. 763977 of the PerTPV project. The authors acknowledge funding from Research Council of Lithuania (grant No. MIP-17-70) and E. Kamarauskas for measurements of ionization potential. Further acknowledgments to Spanish Ministry of Science, Innovation and Universities, MAT2017-88821-R, RTI2018-095362-A-I00, PCI2019-111829-2 and EQC2018-004888-P, and the Comunitat Valenciana, IDIFEDER/2018/061. M.S. acknowledges the Spanish Ministry for his RyC contract.

References

1 H. Ritchie and M. Roser (2019) - "Energy Production & Changing Energy Sources". Published online at OurWorldInData.org. Retrieved from: 'https://ourworldindata.org/energy-production-and-changing-energy-sources' [Online Resource].

2 M. Saliba, J. P. Correa-Baena, M. Graetzel, A. Hagfeldt, A. Abate, Angew. Chem. Int. Ed., 2018, 57, 2554.

3 Z. Shi, A. H. Jayatissa, Materials, 2018, 11, 729

4 Z. Li, T. R. Klein, D. H. Kim, M. Yang, J. J. Berry, M. F. A. M. van Hest, K. Zhu, Nat. Rev. Mater., 2018, 3, 18017.

5 M. A. Green, E. D. Dunlop, J. Hohl-Ebinger, M. Yoshita, N. Kopidakis, A. W.Y. Ho-Baillie, Prog Photovolt: Res Appl., 2020, 28, 3.

6 Q. Jiang, L. Zhang, H. Wang, X. Yang, J. Meng, H. Liu, Z. Yin, J. Wu, X. Zhang, J. You, Nat. Energy, 2016, 2, 16177.

7 E. H. Jung, N. J. Jeon, E. Y. Park, C. S. Moon, T. J. Shin, T. Y. Yang, J. H. Noh, J. Seo, Nature, 2019, 567, 511.

8 M. M. Lee, J. Teuscher, T. Miyasaka, T. N. Murakami, H. J. Snaith, Science, 2012, 338, 643.

9 H. S. Kim, C. R. Lee, J. H. Im, K. B. Lee, T. Moehl, A. Marchioro, S. J. Moon, R. Humphry-Baker, J. H. Yum, J. E. Moser, M. Gratzel, N. G. Park, Sci Rep., 2012, 2, 591.

10 H. Li, K. Fu, A. Hagfeldt, M. Gratzel, S. G. Mhaisalkar, A. C. Grimsdale, Angew. Chem. Int. Ed., 2014, 53, 4085.

11 M. Saliba, J. P Correa-Baena, C. H. Wolff, M. Stolterfoht, N. Phung, S. Albrecht, D. Neher, A. Abate, Chem. Mater., 2018, 30, 4193.

12 J. Zhao, X. Zheng, Y. Deng, T. Li, Y. Shao, A. Gruverman, J. Shield, J. Huang, Energy Environ. Sci., 2016, 9, 3650.

13 K. Jäger, L. Korte, B. Rech, S. Albrecht, Opt. Express, 2017, 25, A473.

14 K. A. Bush, A. F. Palmstrom, Z. J. Yu, M. Boccard, R. Cheacharoen, J. P. Mailoa, D. P. McMeekin, R. L. Z. Hoye, C. D. Bailie, T. Leijtens, I. M. Peters, M. C. Minichetti, N. Rolston, R. Prasanna, S. Sofia, D. Harwood, W. Ma, F. Moghadam, H. J. Snaith, T. Buonassisi, Z. C. Holman, S. F. Bent, M. D. McGehee, Nat. Energy, 2017, 2, 17009.

15 D. Zhao, M. Sexton, H. Y. Park, G. Baure, J. C. Nino, F. So, Adv. Energy Mater., 2014, 5, 1401855.

16 J. T.-W. Wang, Z. Wang, S. Pathak, W. Zhang, D. W. deQuilettes, F. Wisnivesky-Rocca-Rivarola, J. Huang, P. K. Nayak, J. B. Patel, H. A. Mohd Yusof, Y. Vaynzof, R. Zhu, I. Ramirez, J. Zhang, C. Ducati, C. Grovenor, M. B. Johnston, D. S. Ginger, R. J. Nicholas, H. J. Snaith. Energy Environ. Sci., 2016, 9, 2892.

17 J. H. Heo, H. J. Han, D. Kim, T. K. Ahn, S. H. Im, Energy Environ. Sci., 2015, 8, 1602.

18 M. Stolterfoht, C. M. Wolff, Y. Amir, A. Paulke, L. Perdigón-Toro, P. Caprioglio, D. Neher, Energy Environ. Sci., 2017, 10, 1530.

19 C. G. Wu, C.-H. Chiang, Z.-L. Tseng, M. K. Nazeeruddin, A. Hagfeldt, M. Grätzel, Energy Environ. Sci., 2015, 8, 2725.

20 R. Rajeswari, M. Mrinalini, S. Prasanthkumar, L. Giribabu, Chem. Rec., 2017, 17, 1.

21 C. Zuo, L. Ding, Small, 2015, 11, 5528.

22 J. H. Kim, P.W. Liang, S.T. Williams, N. Cho, C. C. Chueh, M. S. Glaz, D. S. Ginger and A. K.Y. Jen, Adv. Mater., 2014, 27, 695.

23 J. Ávila, C. Momblona, P.P. Boix, M. Sessolo, H. J. Bolink, Joule, 2017, 1, 431.

24 J. Ávila, C. Momblona, P.P. Boix, M. Sessolo, M. Anaya, G. Lozano, K. Vandewal, H. Míguez, H. J. Bolink, Energy Environ. Sci., 2018, 11, 3292.

25 C. Momblona, L. Gil-Escrig, E. Bandiello, E. M. Hutter, M. Sessolo, K. Lederer, J. Blochwitz-Nimoth, H. J. Bolink, Energy Environ. Sci. 2016, 9, 3456.

26 G. Bubniene, T. Malinauskas, M. Daskeviciene, V. Jankauskas, V. Getautis, Tetrahedron, 2010, 66, 3199.

27 Y J. Clayden, N. Greeves, S. Warren, Organic chemistry second edition, Oxford university press, 2012.

28 M. C. Alonso Garcia, J. L. Balenzategui, Renewable Energy, 2004, 29, 1997.

29 D. Vaitukaityte, Z. Wang, T. Malinauskas, A. Magomedov, G. Bubniene, V. Jankauskas, V. Getautis, Henry J. Snaith, Adv. Mater. 2018, 30, 1803735.

30 A. Sakalyte, J. Simokaitiene, A. Tomkeviciene, J. Keruckas, G. Buika, J. V. Grazulevicius, V. Jankauskas, C. P. Hsu, Chou-Hsun Yang, J. Phys. Chem. C., 2011, 115, 4856.

31 W. Zhou, Z. Wen, P. Gao, Adv. Energy Mater., 2018, 8, 1702512.

32 T. Malinauskas, M. Daskeviciene, G. Bubniene, I. Petrikyte, S. Raisys, K. Kazlauskas, V. Gaidelis, V. Jankauskas, R. Maldzius, S. Jursenas, V. Getautis, Chem. Eur. J., 2013, 19, 15044.

33 A. Babaei, C. Dreessen, M. Sessolo, H. J. Bolink, RSC Adv., 2020, 10, 6640.

34 A. Babaei, K. P. S. Zanoni, L. Gil-Escrig, D. Pérez-del-Rey, P. P. Boix, M. Sessolo, H. J. Bolink, Front. Chem., 2020, 7, 936.

35 S. van Reenen, M. Kemerink, H. J. Snaith, J. Phys. Chem. Lett. 2015, 6, 3808.

36 B. Danekamp, N. Droseros, D. Tsokkou, V. Brehm, P. P. Boix, M. Sessolo, N. Banerji, H. J. Bolink, J. Mater. Chem. C., 2019, 7, 523.

37 R. A. Belisle, P. Jain, R. Prasanna, T. Leijtens, M. D. McGehee, ACS Energy Lett., 2016, 1, 556.

38 C. M. Wolff, P. Caprioglio, M. Stolterfoht, Dieter Neher, Adv. Mater., 2019, 31, 1902762.

39 J. Endres, D. A. Egger, M. Kulbak, R. A. Kerner, L. Zhao, S. H. Silver, G. Hodes, B. P. Rand, D. Cahen, L. Kronik, A. Kahn, J. Phys. Chem. Lett., 2016, 7, 2722.

40 D. Perez-del-Rey, L. Gil-Escrig, K. P. S. Zanoni, C. Dreessen, M. Sessolo, P. P. Boix, H. J. Bolink, Chem. Mater., 2019, 31, 6945.

41 T. P. Osedach, T. L. Andrew, V. Bulovic, Energy Environ. Sci., 2013, 6, 711.

42 M. L. Petrus, T. Bein, T. J. Dingemans, P. Docampo, J. Mater. Chem. A, 2015, 3, 12159.

43 C. Yin, J. Lu, Y. Xu, Y. Yun, K. Wang, J. Li, L. Jiang, J. Sun, A.D. Scully, F. Huang, J. Zhong, J. Wang, Y.-B. Cheng, T. Qin, W. Huang, Adv. Energy Mater. 2018, 8, 1800538.

44 M. Degbia, M. Ben Manaa, B. Schmaltz, N. Berton, J. Boucle, R. Antony, F. Tran Van, Mater. Sci. Semicond. Process., 2016, 43, 90.

45 O. Usluer, M. Cloutet, G. Hadziioannou, ACS Macro Lett., 2014, 3, 1134.

Supplementary information

Enamine-based hole transporting materials for vacuum-deposited perovskite solar cells

Matas Steponaitis[a], Maria-Grazia La-Placa[c], İsmail Cihan Kaya[c], Giedre Bubniene[a], Vygintas Jankauskas[b], Maryte Daskeviciene[a], Michele Sessolo[c], Tadas Malinauskas[a]*, Henk J. Bolink[c] and Vytautas Getautis[a].*

[a] Department of Organic Chemistry, Kaunas University of Technology, Radvilenu pl. 19, LT-50254, Kaunas, Lithuania

[b] Institute of Chemical Physics, Vilnius University Sauletekio al.3, Vilnius LT-10257, Lithuania

[c] Instituto de Ciencia Molecular, Universidad de Valencia, C/Catedrático J. Beltrán 2, 46980 Paterna, Spain

*Corresponding authors

michele.sessolo@uv.es, tadas.malinauskas@ktu.lt

Experimental details

General

Chemicals were purchased from Sigma-Aldrich and TCI Europe and used as received without further purification. The course of the reactions was monitored by TLC (thin layer

chromatography) on ALUGRAM SIL G/UV254 plates and developed with UV light. Silica gel (grade 9385, 230–400 mesh, 60 Å, Aldrich) was used for column chromatography. The 1H and 13C NMR spectra were taken on Bruker Avance III 400 (400 MHz) spectrometer at room temperature. The chemical shifts, expressed in δ (ppm) are relative to a (CH3)4Si (TMS, 0 ppm) internal standard. Elemental analysis was performed with an Exeter Analytical CE-440 elemental analyzer, Model 440 C/H/N/. Thermogravimetric analysis (TGA) was performed on a Q50 thermogravimetric analyzer (TA Instruments) at a scan rate of 10 K min-1 in the nitrogen atmosphere. Differential scanning calorimetry (DSC) was performed on a Q10 calorimeter (TA Instruments) at a heating rate of 10 K/min in the nitrogen atmosphere. The glass transition temperatures for the investigated compounds were determined during the second heating scan. Melting point for crystalline materials were observed using Mel-Temp DigiMelt MPA 161 melting point apparatus at a heating rate 1 C°/min.

Optical measurements

Absorption spectra of the dilute solutions in toluene (concentration 10^{-4} M) and on glass substrate were recorded on a UV/Vis–NIR spectrophotometer, Lambda 35 (Perkin–Elmer). Fluorescence of the investigated compounds in toluene (concentration 10^{-5} M) and on glass substrate were recorded on Edinburgh Instruments fluorescence spectrophotometer FLS920.

Ionization energy measurements (*IE*)

The ionization energy of the layers of the synthesized compounds was measured by electron photoemission in air (the error of this method is evaluated as ±0.03eV). The samples were prepared by dissolution in THF and the solutions were coated on Al plates pre-coated with approximately 0.5 μm thickness of a methyl methacrylate and methacrylic acid copolymer adhesive layer. The

thickness of the transporting material layer was 0.5 – 1 μm. The organic materials investigated are stable enough to oxygen that the measurements may be carried out in the presence of air. The samples were illuminated with monochromatic light from a quartz monochromator fitted with a deuterium lamp. The power of the incident light beam was $(2–5)\cdot10^{-8}$ W. A negative voltage (-330 V) was supplied to the sample substrate. The counter electrode with a 4.5 · 15 mm^2 slit for illumination was placed 8 mm from the sample surface. The counter electrode was connected to the input of the BK2–16 type electrometer, working in the open input regime, for the photocurrent measurement. The 10^{-15} – 10^{-12} A photocurrent (I) flowed in the circuit under illumination. The value of I is strongly dependent on the incident-light photon energy (hν). The dependence $I^{0.5}$ on incident-light quanta energy hν was plotted from the experiment results. Usually the dependence of I on the incident light quantum energy is described well by the linear relationship $I^{0.5} = f(h\nu)$ near the threshold. The linear part of this dependence was extrapolated to the hν axis and the *IE* value was determined as the photon energy at the interception point.

Charge carrier mobility measurements

The samples for the charge carrier mobility measurements were prepared by spin coating solutions of the synthesized compounds in tetrahydrofuran onto PS films with a conductive Al layer. The layer thickness was in the range 5 – 10 μm. The charge drift mobility was measured by XTOF. An electric field was created by positive corona charging. The charge carriers were generated at the layer surface by illumination with pulses of a nitrogen laser (pulse duration = 2 ns, λ = 337 nm). The layer surface potential decrease as a result of pulse illumination was up to 1–5% of the initial potential before illumination. The capacitance probe that was connected to the wide-frequency band electrometer measured the speed of the surface potential decrease (dU/dt). The transit time (t_t) was determined by the kink on the curve of the dU/dt transient on a linear or double logarithmic

scale. The drift mobility was calculated by the formula $\mu = d^2/U_0t_t$ (d is the layer thickness, U_0 is the surface potential at the moment of illumination).

Synthesis of the materials

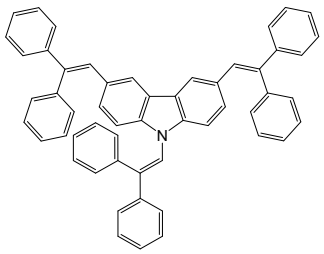

3,6,9-tris(2,2-diphenylvinyl)-9H-carbazole (H1): a mixture of carbazole (1g, 6mmol), diphenylacetaldehyde (3.52g, 18.0mmol) and camphor-10-sulfonic acid (β) (1.39g, 6mmol) were dissolved in toluene (12ml + volume of the Dean-Stark trap). The mixture was heated for 5 hours at reflux. At the end of the reaction (TLC control 1/24 acetone/n-hexane) the mixture was cooled to room temperature and extracted with ethyl acetate. The organic layer was dried over anhydrous Na_2SO_4, filtered and solvent was removed. The crude product was purified by column chromatography (1/24 acetone/n-hexane) to give **H1** as white crystals (m. p. 213-215°C) Yield: 1.8g (42%).

Elemental analysis calcd (%) for $C_{54}H_{39}N$ (701.91g/mol): C 92.40; H 5.60; N 2.00. Found: 92.17; H 5.71; N 2.12.

^{1}H NMR ($CDCl_3$, 400MHz, ppm): δ 7.44 (s, 2H); 7.38-7.16 (m, 25H); 7.11-7.01 (m, 6H), 7.00-6.93 (m, 2H), 6.92-6.82 (m, 4H).

^{13}C NMR ($CDCl_3$, 101MHz, ppm): δ 143.76; 140.74; 140.66; 140.60; 139.63; 138.66; 138.15; 130.52; 129.84; 129.43; 128.80; 128.73; 128.34; 128.25; 128.21; 127.82; 127.72; 127.49; 127.25; 127.19; 123.48; 121.04; 120.29; 110.04.

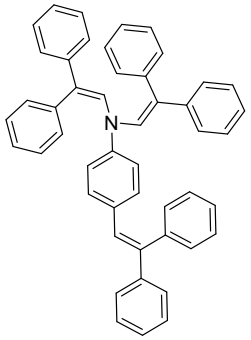

***N,N*,4-tris(2,2-diphenylethenyl)aniline (H2):** a mixture of aniline (0.5g, 5.4mmol), diphenylacetaldehyde (3.45g, 20.1mmol) and camphor-10-sulfonic acid (β) (1.24g, 5.4mmol) were dissolved in THF (10ml + volume of the Dean-Stark trap). The mixture was heated for 6 hours at reflux. At the end of the reaction (TLC control 2/23 toluene/n-hexane) the mixture was cooled to room temperature and extracted with ethyl acetate. The organic layer was dried over anhydrous Na_2SO_4, filtered, the solvent was removed. The crude product was dissolved in 17ml THF and poured into 250ml ethanol to remove the excess amount of aldehyde. The acquired powder was purified by column chromatography (2/23 toluene/n-hexane) to give **H2** as yellow crystals (m. p. 230-232°C). Yield: 1.4g (42%).

Elemental analysis calcd (%) for $C_{48}H_{37}N$ (627.83g/mol): C 91.83; H 5.94; N 2.23. Found: 91.97; H 5.67; N 2.36.

^{1}H NMR ($CDCl_3$, 400MHz, ppm): δ 7.40 – 7.21 (m, 16H); 7.14 – 7.01 (m, 10H); 6.97 (d, J = 8.6 Hz, 3H), 6.87 (d, J = 8.6 Hz, 2H), 6.42 (d, J = 7.5 Hz, 4H), 5.81 (s, 2H).

^{13}C NMR ($CDCl_3$, 101 MHz, ppm) δ 144.33; 143.46; 141.26; 140.74; 140.57; 140.00; 132.37; 131.12; 130.59; 130.25; 129.54; 128.91; 128.61; 128.55; 128.21; 127.73; 127.63; 127.47; 127.44; 127.29; 127.21; 126.77; 116.45.

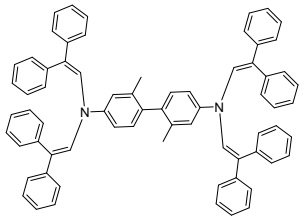

***N*^{4},*N*^{4},*N*$^{4'}$,*N*$^{4'}$-tetrakis(2,2-diphenylethenyl)-2,2'-dimethyl[1,1'-biphenyl]-4,4'-diamine (H3):** a mixture of m-tolidine (0.6g, 2.8mmol), diphenylacetaldehyde (2.66g, 13.6mmol) and camphor-10-sulfonic acid (β) (0.66g, 2.8mmol) were dissolved in toluene (7ml + volume of the Dean-Stark trap). The mixture was heated for 3 hours at reflux. Afterwards (TLC control 1/24 v/v diethyl ether/n-hexane) the reaction mixture was cooled and poured to 130ml of ethyl acetate giving yellow crystals (m. p. 337-339°C) that were filtered and then washed with ethyl acetate and ethanol (1/4 v/v). Yield: 0.94 g (36%).

Elemental analysis calcd (%) for $C_{70}H_{56}N_2$ (925.23g/mol): C 90.87; H 6.10; N 3.03. Found: 90.76; H 5.98; N 3.26.

^{1}H NMR ($CDCl_3$, 400MHz, ppm): δ 7.40 – 7.27 (m, 14H); 7.16 – 7.04 (m, 22H); 7.02-6.96 (m, 4H), 6.52-6.47 (m, 6H), 5.95 (s, 4H), 2.13-2.05 (m, 6H).

^{13}C NMR ($CDCl_3$, 101 MHz, ppm) δ 144.66, 141.57, 140.17, 137.45, 135.25, 131.64, 130.67, 129.67, 129.20, 129.06, 128.55, 127.76, 127.66, 127.15, 126.67, 118.41, 114.62, 20.34.

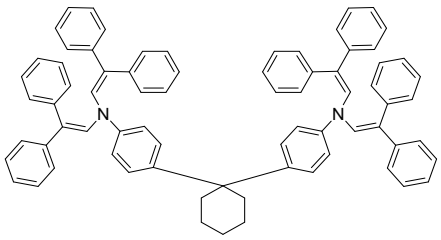

***N1*^{4},*N1*^{4},*N3*^{4},*N3*^{4}-tetrakis(2,2-diphenylethenyl)-2^3,2^4,2^5,2^6-tetrahydro-2^{2}H-[1^1,2^1:2^1,3^1-terphenyl]-1^4,3^4-diamine (H4):** a mixture of 1,1-bis(4-aminophenyl)cyclohexane (1.2g,

4.5mmol), diphenylacetaldehyde (4.4g, 22.5mmol) and camphor-10-sulfonic acid (β) (1.04g, 4.5mmol) were dissolved in THF (9ml + volume of the Dean-Stark trap). The mixture was heated for 4 hours at reflux. Afterwards (TLC control 2/23 v/v diethyl ether/n-hexane) the reaction mixture was cooled and poured to 180ml of methanol giving yellow amorphous mass that was filtered and then washed with methanol. The crude product was purified by column chromatography (2/23 v/v diethyl ether/n-hexane) to give **H4** as yellow crystals (m. p. 308-310°C). Yield: 1.8g (41%).

Elemental analysis calcd (%) for $C_{74}H_{62}N_2$ (979.32g/mol): C 90.76; H 6.38; N 2.86. Found: 90.63; H 6.24; N 3.13.

^{1}H NMR ($CDCl_3$, 400MHz, ppm): δ 7.32 – 7.26 (m, 12H); 7.24 – 7.20 (m, 4H); 7.14-7.00 (m, 24H), 6.48-6.44 (m, 8H), 5.88 (s, 4H), 2.27 (s, 4H) 1.62-1.48 (m, 6H).

^{13}C NMR ($CDCl_3$, 101 MHz, ppm) δ 143.15, 142.25, 141.57, 140.11, 131.39, 129.64, 129.00, 128.48, 127.86, 127.70, 127.60, 127.06, 126.56, 117.20, 45.32, 37.30, 26.46, 22.93.

Device fabrication and characterization

Photolithographically patterned ITO-coated glass substrates were used as substrates. MoO_3 and 2,9-Dimethyl-4,7-diphenyl-1,10-phenanthroline (BCP) were purchased from Lumtec, fullerene (C60) was purchased from Sigma Aldrich. CH_3NH_3I (MAI) and PbI2 were purchased from Lumtec. All materials were used as received.

ITO-coated glass substrates were subsequently cleaned with soap, water and isopropanol in an ultrasonic bath, followed by UV-ozone treatment. They were transferred to a vacuum chamber integrated into a nitrogen-filled glovebox (H_2O and O_2 < 0.1 ppm) and evacuated to a pressure of 10^{-6} mbar. The vacuum chamber used to sublime the HTMs, ETL and MAPI is equipped with six

temperature-controlled evaporation sources (Creaphys) fitted with ceramic crucibles. The sources were directed upward with an angle of approximately 90° with respect to the bottom of the evaporator. The substrate holder to evaporation source distance is approximately 20 cm. Three quartz crystal microbalance (QCM) sensors were used: two monitoring the deposition rate of each evaporation source and a third one close to the substrate holder monitoring the total deposition rate. The materials were sublimed and the evaporation rate was controlled by separate QCM sensors obtaining precisely the deposited thickness. For the perovskite deposition, MAI and PbI_2 were coevaporated by measuring the deposition rate of each material in a different sensor and obtaining the total perovskite thickness in the third one, leading to a 500 nm-thick film. MoO_3 and Ag were evaporated in a third vacuum chamber using tantalum boats by applying currents ranging from 2.0 to 4.8 A.

The J–V curves of the solar cells were recorded using a Keithley 2612A Source-Meter with 0.01 V steps and integrating the signal for 20 ms after a 10 ms delay, corresponding to a speed of about 0.3 V s^{-1}. The devices were illuminated under a Wavelabs Sinus 70 LED solar simulator. The light intensity was calibrated before every measurement using a calibrated Si reference diode. Solar cell stability measurements were recorded using a maximum power point tracking system, with a white LED light source at 1 sun equivalent, developed by Candlelight. During the stability measurements, the encapsulated devices were exposed to a flow of N_2 gas; temperature was stabilized at 300 K during the entire measurement using a water-circulating cooling system controlled by a Peltier element; J–V curves were recorded every 10 min.

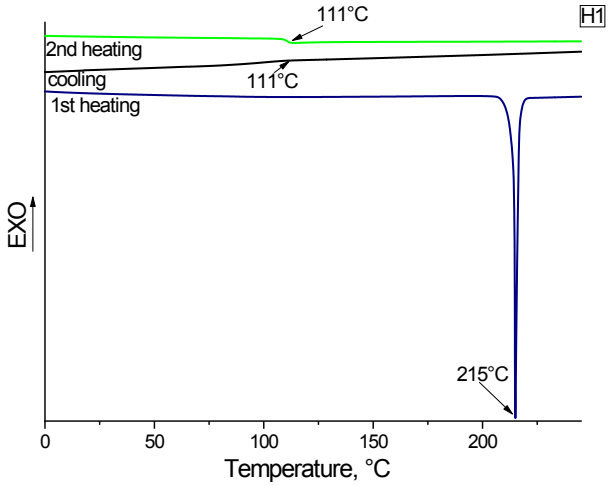
H1
111°C
2nd heating
cooling
111°C
1st heating
EXO
215°C
0
50
100
150
200
Temperature, °C

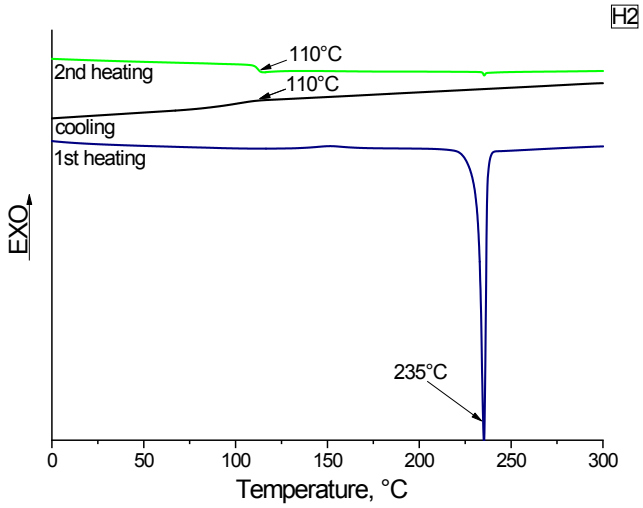
H2
110°C
2nd heating
110°C
cooling
1st heating
EXO
235°C
0
50
100
150
200
250
300
Temperature, °C

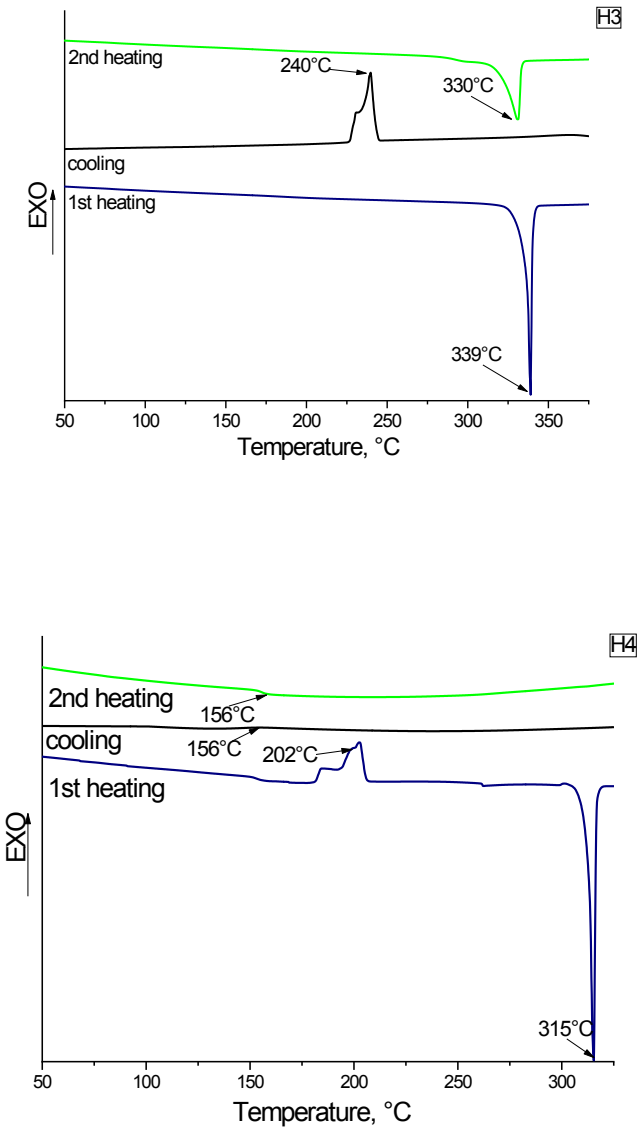

Figure **S1**. DSC graphs of HTMs **H1**, **H2**, **H3** and **H4**.

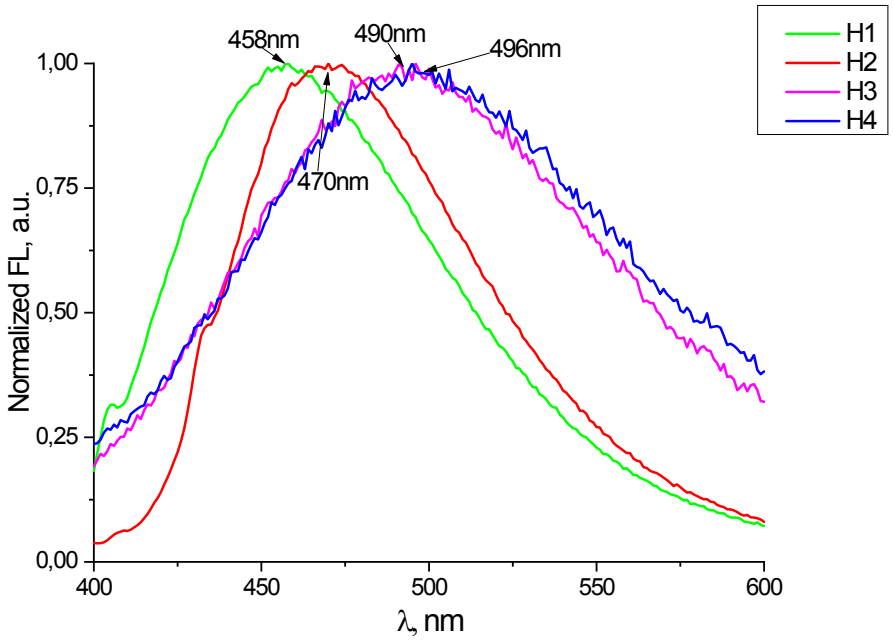

Figure S2. H1, **H2**, **H3**, **H4** fluorescence spectra in toluene. For **H1** λ_{ex}=360nm, **H2** λ_{ex}=382nm. **H3** and **H4** λ_{ex}=345nm.

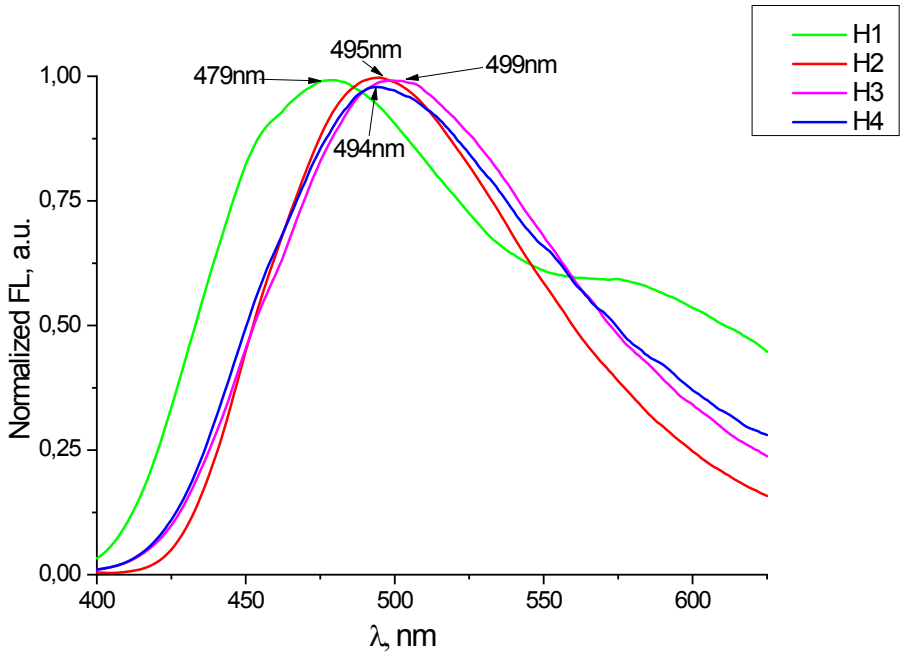

Figure S3. HTM fluorescence spectra on glass substrate. For **H1** (λ_{ex}=360nm), **H2** (λ_{ex}=382nm), **H3** and **H4** (λ_{ex}=345nm).

Cost estimation

In order to estimate the cost, data have been collected from chemical suppliers (Sigma-Aldrich, TCI, Acros Organics, Fischer Chemicals, Oakwood Chemical and Eurochemicals) for all used chemicals. The cost of HTM **H2** was calculated in February 2020, while the cost of the synthesis of Spiro-TTB, in November 2019.

Table S1. Materials, quantities and cost for the synthesis of **H2**.

Chemicals	Weight reagent (g/g)	Weight solvent (g/g)	Weight Workup (g/g)	Price of chemicals (€/kg)	Cost of chemical (€/g product)	Total cost (€/g)
Aniline	0.36			36.42	0.00	
Diphenylacetaldehyde	2.8			3578.52	10.02	
10-Camphorsulfonic acid	0.9			260.0	0.23	
THF		20	17	8.88	0.33	
Ethyl acetate			125	2.85	0.35	
Ethanol			250	6.08	1.52	
Toluene			80	2.46	0.20	
Hexane			920	3.16	2.90	

Silica gel			100	18.60	1.86	
Na_2SO_4			20	6.08	0.12	
H2	4.06	20	1617			17.53

17.53€=19.23$

Table S2. Materials quantities and cost for the synthesis of Spiro-TTB.

Chemicals	Weight reagent (g/g)	Weight solvent (g/g)	Weight Workup (g/g)	Price of chemicals ($/kg)	Cost of chemical ($/g product)	Cost per step ($/step)
2-Bromoanline	0.99			706.70	0.70	
Hydrochloric acid	3.49			62.60	0.22	
$NaNO_2$	0.48			31.66	0.02	
Potassium iodide	1.43			108.35	0.15	
Acetonitrile		12.38		6.08	0.08	
Dichloromethane			295	11.16	3.29	
$MgSO_4$			2	54.24	0.08	
2-Bromoiodobenzene	**6.39**	**12.38**	**297**			**4.54**
Phenylboronic acid	0.67			1419.73	0.96	
K_2CO_3	1.83			6.74	0.01	
$PdCl_2(PPh_3)_2$	0.06			16701.40	0.93	
Dimethoxyethane		13.49		94.77	1.28	
Diethyl ether			159	22.89	3.63	

$MgSO_4$			2	54.24	0.08	
Heptane			284	4.59	1.30	
Ethyl acetate			160	3.63	0.58	
Silica gel			390	44.41	17.34	
2-Bromobiphenyl	**2.56**	**13.49**	**995**			**26.11**
9-Fluorenone	0.87			162.72	0.14	
Magnesium	0.13			36.32	0.00	
Tetrahydrofuran		3.17		6.94	0.03	
Methanol			136	2.21	0.30	
Hydrochloric acid (5%)			19	3.13	0.06	
Acetic acid			90	40.12	3.63	
9,9'-Spirobi[9*H*-fluorene]	**1**	**3.17**	**245**			**4.16**
Iodic acid	1.2			371.09	0.44	
Sulfuric acid		0.31		74.74	0.02	
Acetic acid		14		40.12	0.56	
Potassium hydroxide			0.14	21.21	0.00	
Toluene			142	4.08	0.58	

2,2',7,7'-Tetraiodo-9,9'-spirobifluorene	**1.2**	**14.31**	**142.14**			**1.6**
Potassium *t*-butoxide	1.05			1.05	0.16	
$Pd(OAc)_2$	0.012			44499.40	0.53	
$P(tBu)_3$	0.022			53053.50	1.17	
Toluene		12		4.08	0.05	
Dichloromethane			728	11.16	8.12	
Na_2SO_4			1	12.79	0.01	
Ethyl acetate			2	3.63	0.01	
Silica gel			263	66.41	17.47	
4,4′-Dimethyldiphenylamine	1.057			2800	2.96	
Total	**13.291**	**55.35**	**2673.14**			**66.89**

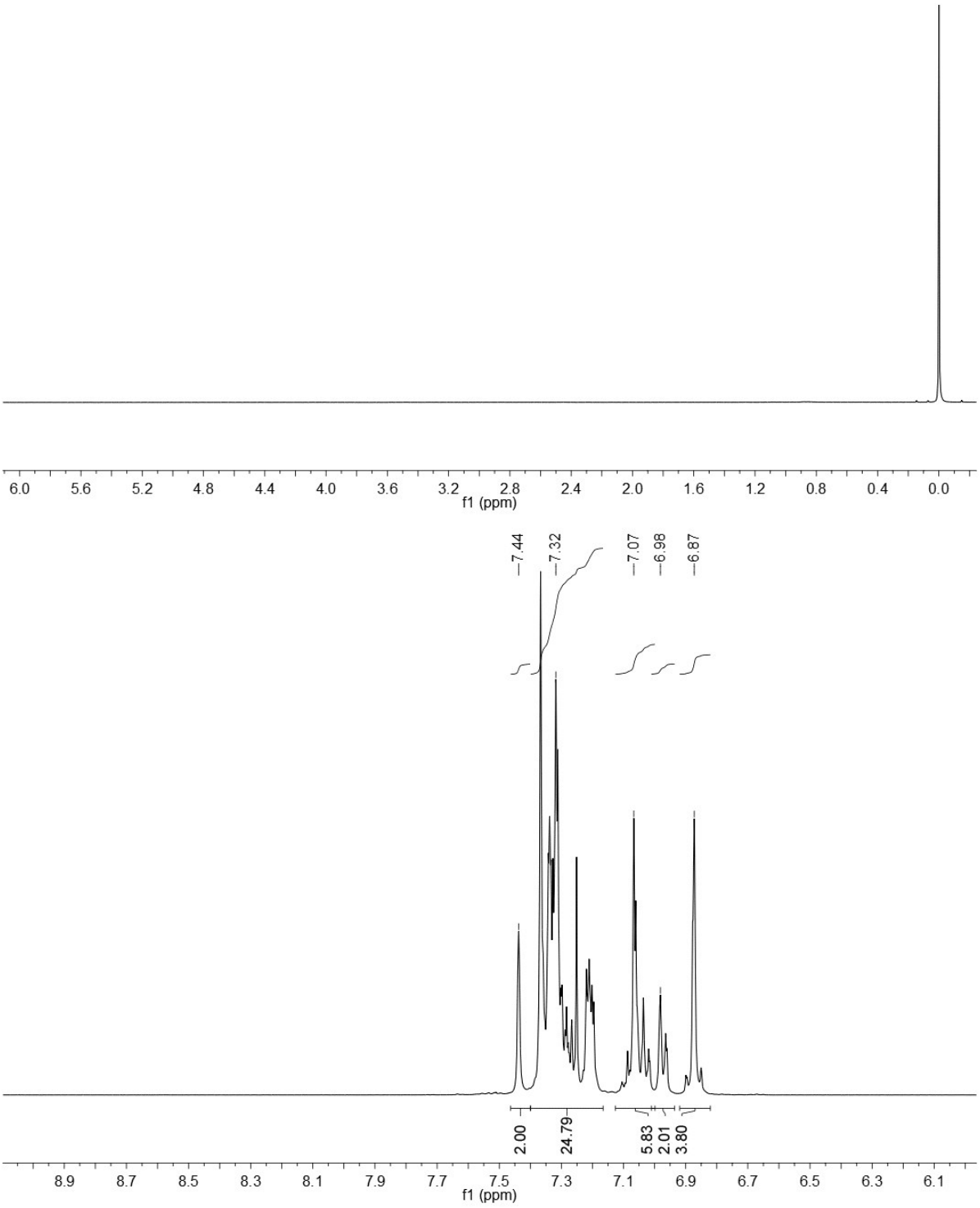

Figure S4. *3,6,9-tris(2,2-diphenylvinyl)-9H-carbazole (H1)* ^{1}H *NMR (400 MHz,* $CDCl_3$*, δ, ppm).*

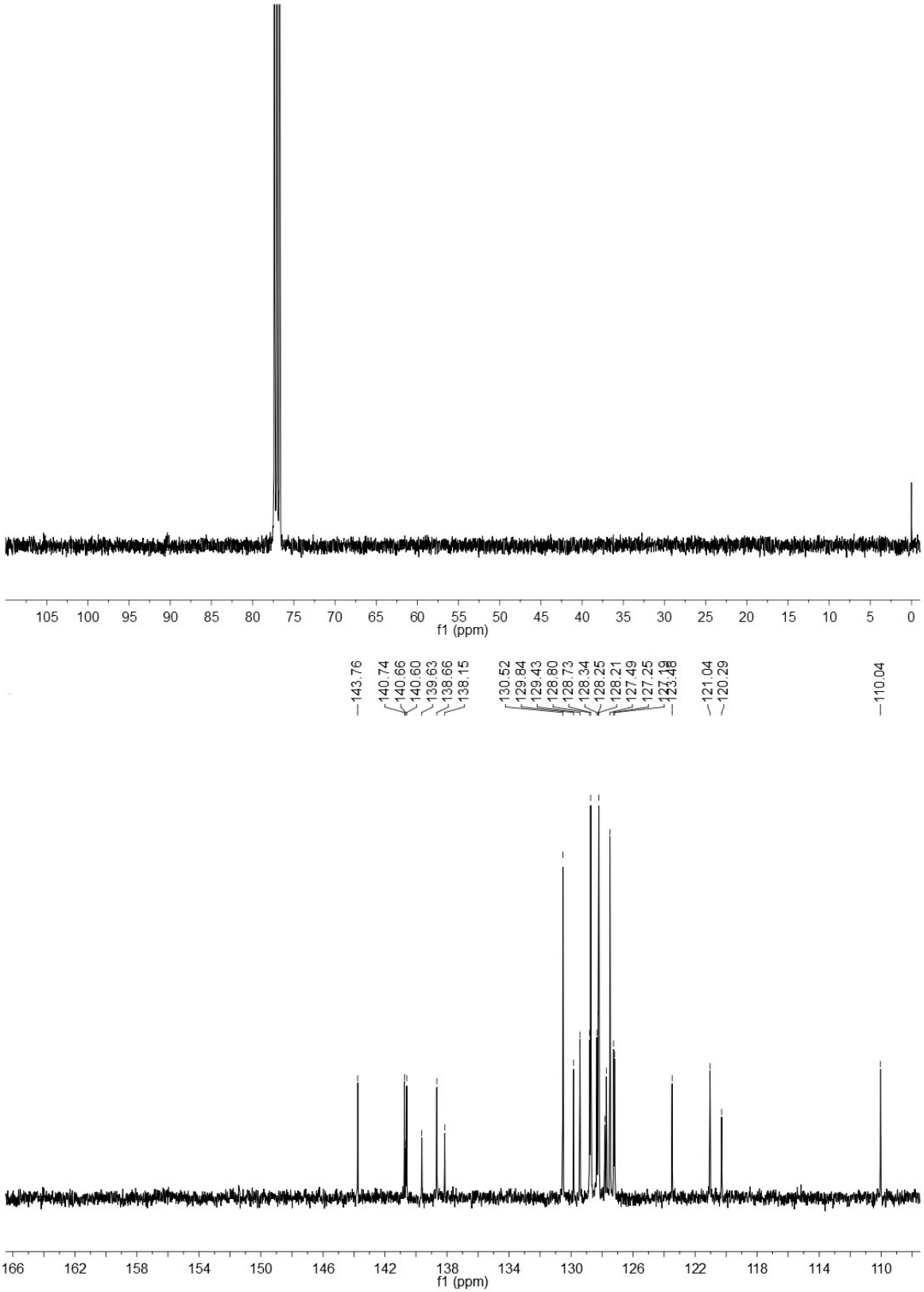

Figure S5. *3,6,9-tris(2,2-diphenylvinyl)-9H-carbazole (H1)* ^{13}C *NMR (101 MHz,* $CDCl_3$*, δ, ppm).*

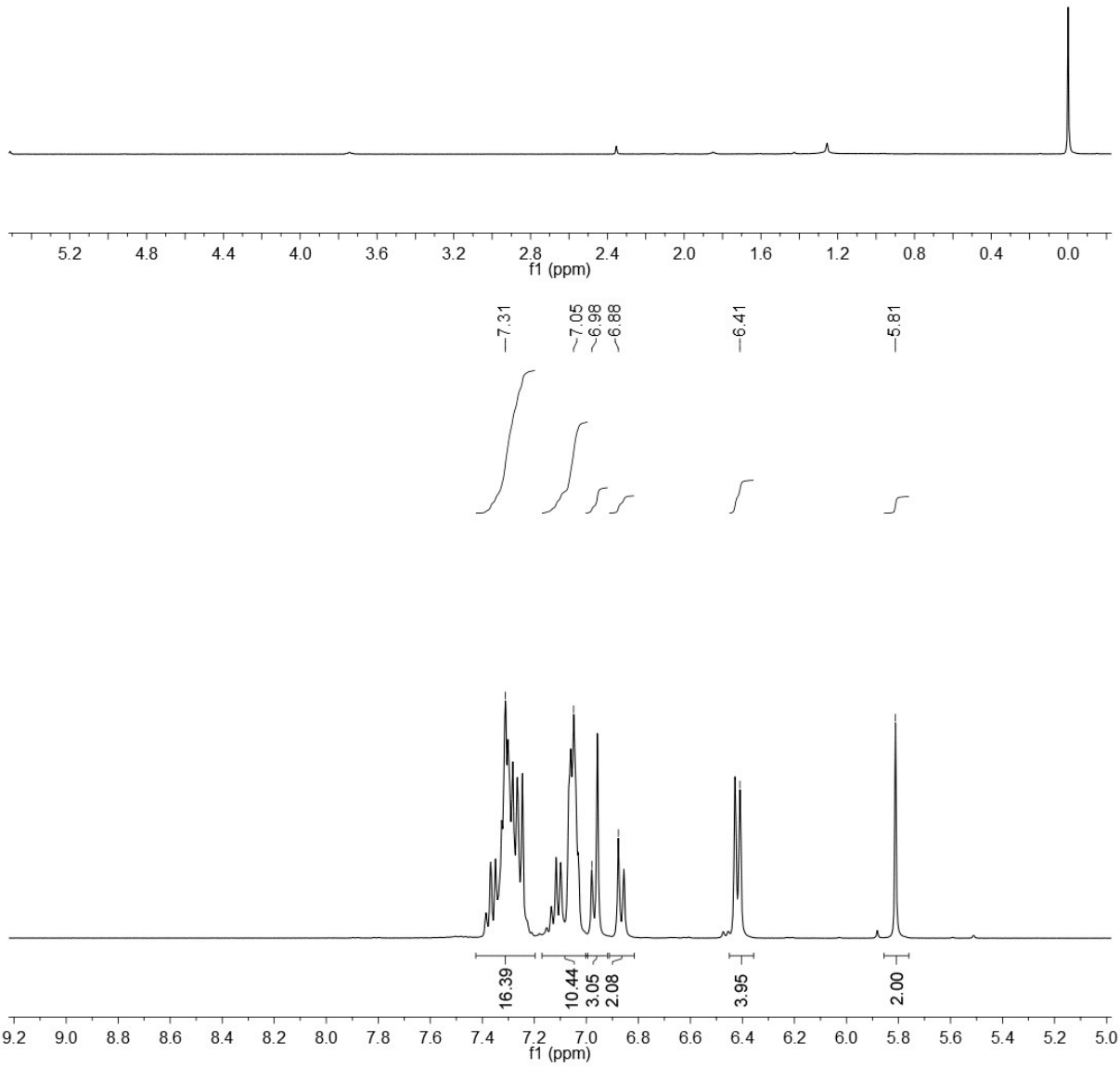

Figure S6. *N,N,4-tris(2,2-diphenylethenyl)aniline (H2)* ^{1}H *NMR (400 MHz,* $CDCl_3$*, δ, ppm).*

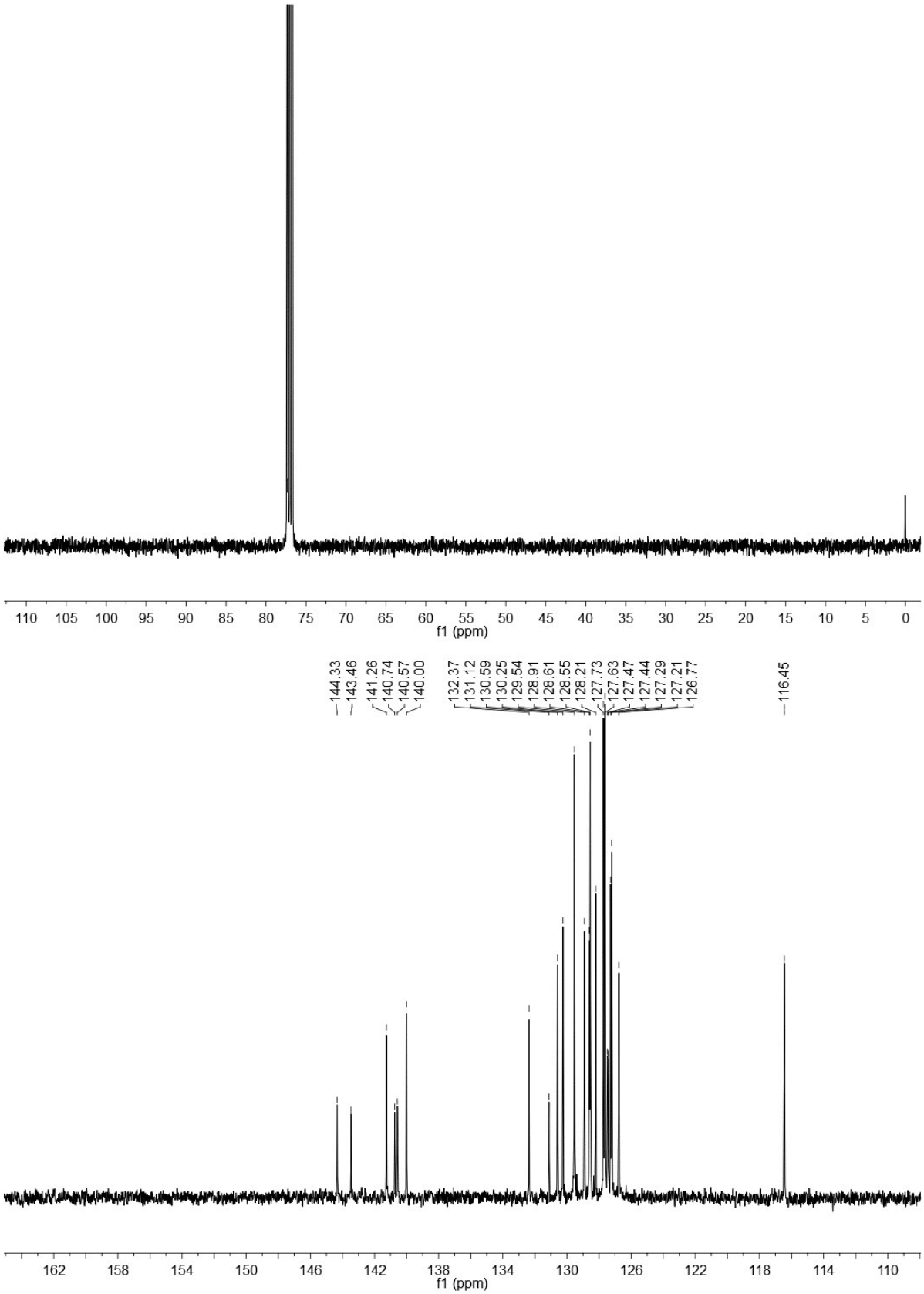

Figure S7. *N,N,4-tris(2,2-diphenylethenyl)aniline (H2)* ^{13}C *NMR (101 MHz,* $CDCl_3$*, δ, ppm).*

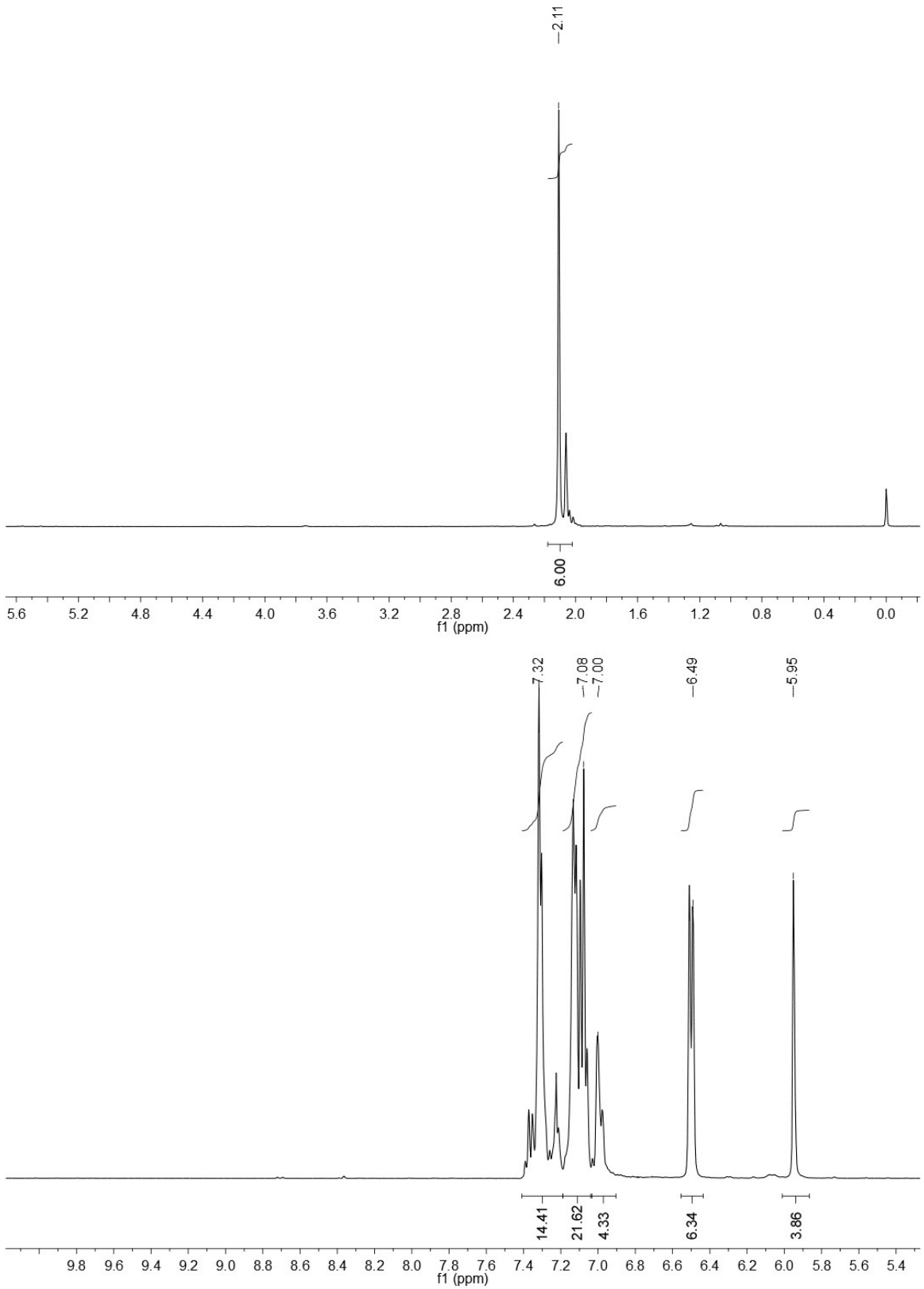

Figure S8. *$N^4,N^4,N^{4'},N^{4'}$-tetrakis(2,2-diphenylethenyl)-2,2'-dimethyl[1,1'-biphenyl]-4,4'-diamine (H3) ^1H NMR (400 MHz, $CDCl_3$, δ, ppm).*

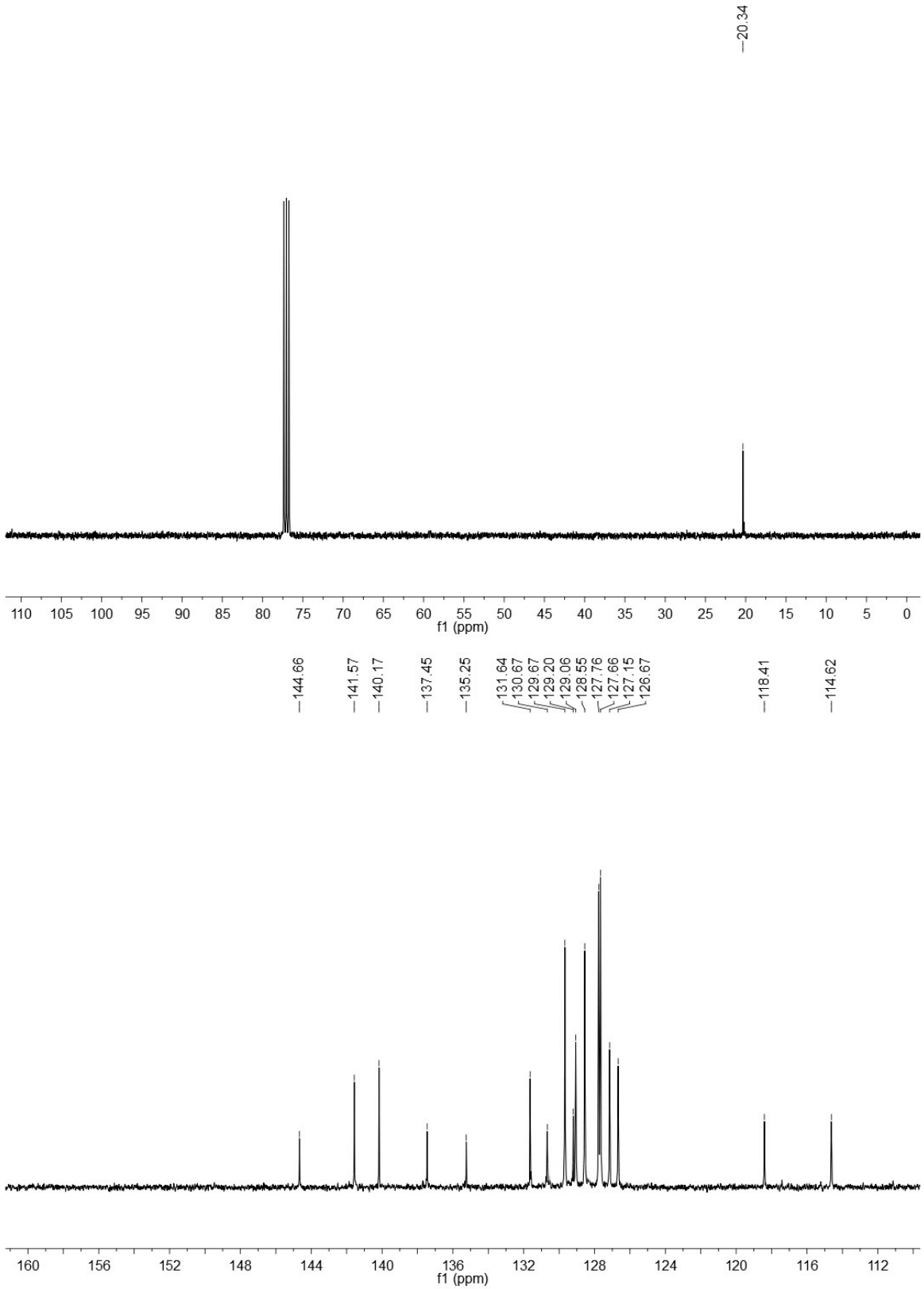

Figure S9. *$N^4,N^4,N^{4'},N^{4'}$-tetrakis(2,2-diphenylethenyl)-2,2'-dimethyl[1,1'-biphenyl]-4,4'-diamine (H3) ^{13}C NMR (101 MHz, $CDCl_3$, δ, ppm).*

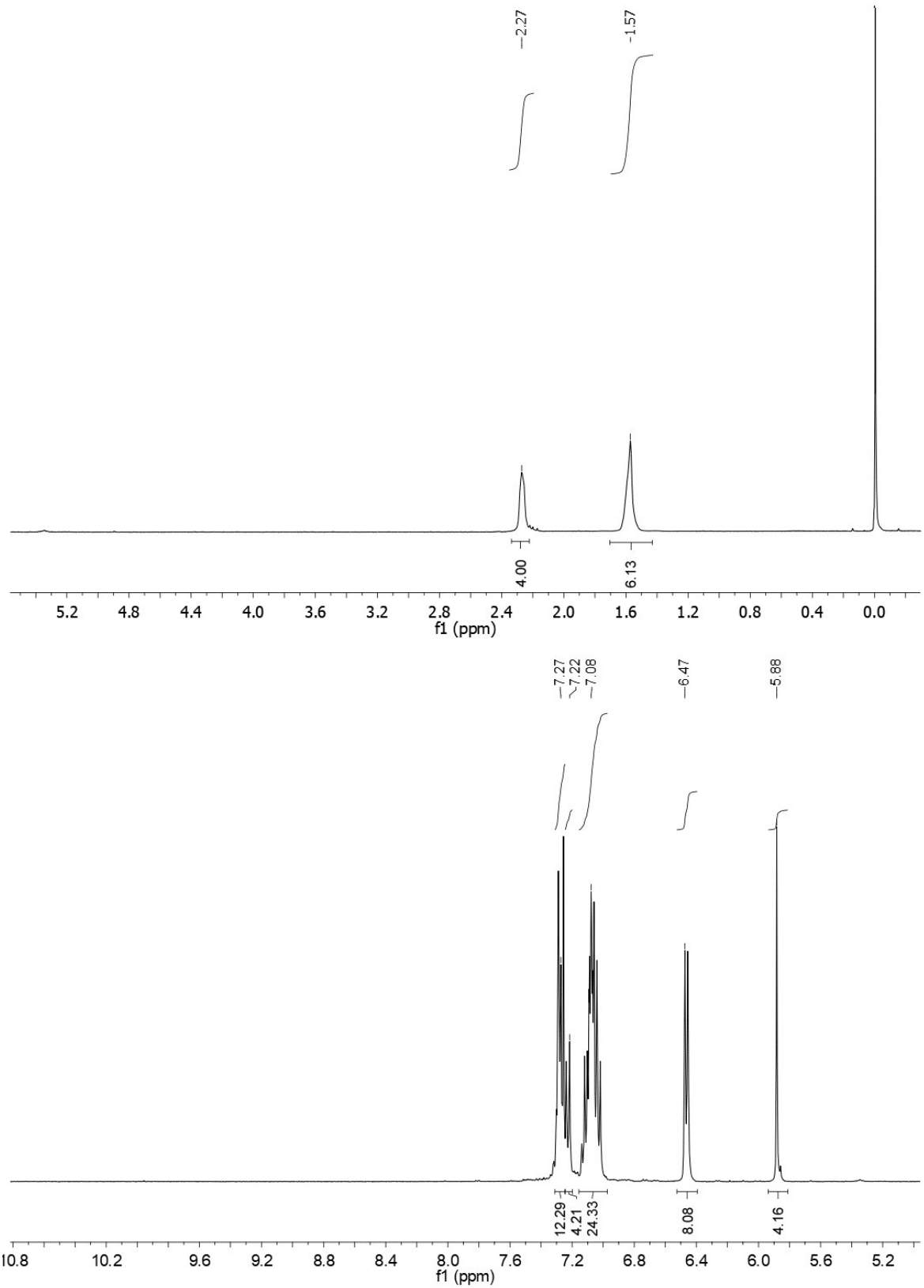

Figure S10. *$N1^4,N1^4,N3^4,N3^4$-tetrakis(2,2-diphenylethenyl)-$2^3,2^4,2^5,2^6$-tetrahydro-2^2H-[$1^1,2^1$:$2^1,3^1$-terphenyl]-$1^4,3^4$-diamine (H4) ^{1}H NMR (400 MHz, $CDCl_3$, δ, ppm).*

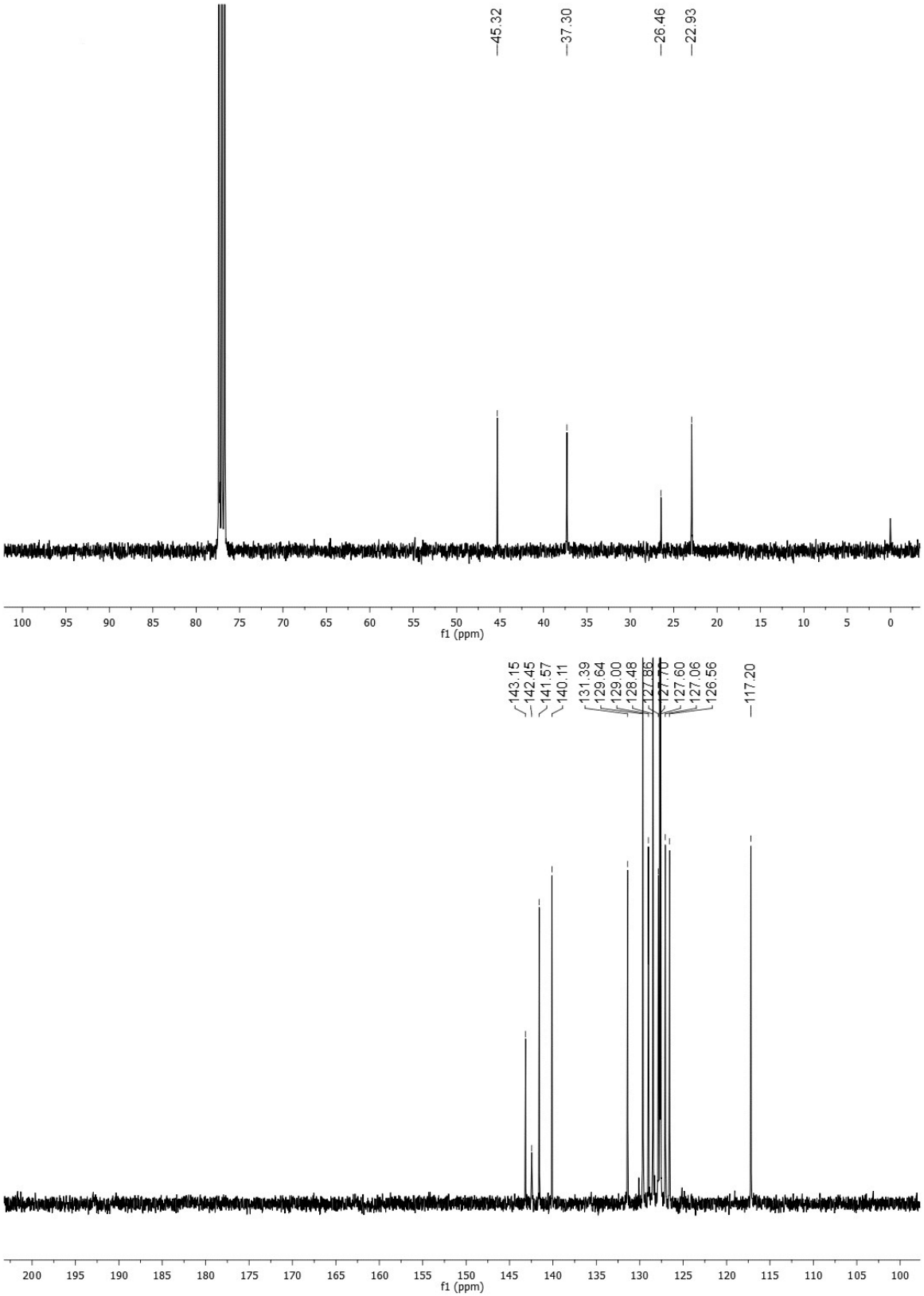

Figure S11. *$N1^4,N1^4,N3^4,N3^4$-tetrakis(2,2-diphenylethenyl)-$2^3,2^4,2^5,2^6$-tetrahydro-2^2H-[$1^1,2^1$:$2^1,3^1$-terphenyl]-$1^4,3^4$-diamine (H4) ^{13}C NMR (101 MHz, $CDCl_3$, δ, ppm).*